*

https://doi.org/10.1016/j.jallcom.2020.153930

Entropy stabilized single-phase (Hf,Nb,Ta,Ti,Zr)B_2 solid solution powders obtained via carbo/boro-thermal reduction

Frédéric Monteverde, Federico Saraga

*National Research Council of Italy, Institute of Science and Technology for Ceramics, Faenza, 48018 RA, Italy

Abstract

This report deals with the synthesis of entropy stabilized (ES) single-phase (Hf,Nb,Ta,Ti,Zr)B_2 powders, with specific surface area of about 1.6 m^2/g, in a AlB_2-type structure using individual transition metal (TM) oxides and, for the first time, elemental boron and carbon as precursors to feed the carbo/boro-thermal (CBT) reduction. Elemental B and C were intimately mixed into a mixture of five TM oxide powders, TM= Hf, Nb, Ta, Ti and Zr through an high energy planetary milling. ES single-phase TM diboride solid solution powders were obtained by a synthesis process consisting of a CBT reduction followed by solid solution formation. A B:C molar ratio=1.27 (per one molar mass of metals) was adjusted leading the CBT reduction to completion (i.e., full conversion of TM oxides), applying the synthesis temperature of 2123 K under vacuum. The micro-strain intended as deviation of some inter-planar distances of the entropy stabilized AlB_2-type solid solution lattice, was analyzed by x-ray diffraction: a strong anisotropic micro-strain was found, and was attributed to the compositional disorder due to the coexistence of differing TM with different atomic radius.

Keywords: ultra-high temperature ceramics, solid solution, carbo/boro-thermal reduction, micro-strain.

Corresponding Author: frederic.monteverde@istec.cnr.it

1.Introduction

The rare dual combination of ceramic-like and metallic-like properties makes ultra-high temperature ceramics (UHTCs) very attractive to fill the gap of unmet requirements of some demanding applications (high speed machining, neutron or concentrated solar radiation, etc.), that the existing structural materials are not able to fulfill [1]. Moreover UHTCs, most remarkably borides and carbides of transition metals, have attracted much attention for potential use in thermal protection applications for hypersonic aerospace and atmospheric re-entry vehicles due to melting temperatures exceeding 3273 K, which make them candidates to withstand service conditions amongst the harshest known [2]. However, the propensity of UHTCs to react with oxygen has led the scientific community to address this limitation through intentional second phase additions. On one end, the widely used silicon carbide was added to metal diborides (MeB_2) to protect them by forming oxygen diffusion barriers made of borosilicate glasses [3]. On the other end, prolonged protection provided by viscous glasses over 2000 K, especially in fast flying conditions [4], is not fully affordable because molten glasses easily shear off: the underlying UHTCs, bulk or coating, are left unprotected, at the mercy of a severe oxidation attack.

In recent five years, on the wave of research and development of advanced materials engineered via the entropy stabilization (ES) approach, novel ceramics ranging from oxides [5] [6], carbides [7] [8], nitrides [9] to borides [10] or silicides [11] have shown the potential to found a new paradigm in the design of materials for a spectrum of applications not yet fully understood. ES materials are currently recognized as “high-entropy” materials. The term “high-entropy”, to personal opinion of the authors, does deviate the attention from the stabilization of new materials via augmented levels of configurational entropy. The term “high-entropy” is derived from the formation of alloys containing at least four principal elements in roughly equimolar amounts [12].

Entropy stabilized ceramics, whatever declined as oxides, carbides or borides, can be described as solid solutions (SS) of multi-principal components in near-equi-atomic ratios with increased configurational entropy stabilized at high temperature in new and simple structures [13].

The search for new materials via entropy engineering has also fostered the appeal of the UHTC scientific community. In particular, much attention has been switched towards a group of advanced materials already identified in historic studies [14] based on MeB_2, Me= Hf, Ta, Ti or Zr. In this regard, H. Chen *et al*., very recently reported a novel strategy toward making multicomponent thermal barriers, widening the potential of the entropy engineering approach [15].

Regarding the resistance to oxidation, key question is whether all components in solid solution of non-oxide ES ceramics (but the question can more generally be extended to ES materials) react with oxygen simultaneously, or otherwise oxidation prefers taking place selectively. In this respect, the recent work of B. Ye and co-authors seems to confirm such a reasoning [16]. Besides, Backman L. *et al*., showed that, due to large differences in the relative thermodynamic stability of the new formed oxides, that selective oxidation may occur, i.e., that the resulting oxide scale would be governed by their relative thermodynamic stability and the rate controlling kinetics, leading to the depletion of those components from the underlying bulk [17].

First-principle studies and ab-initio modeling may predict the energetically most favored multicomponent systems. In this regard such tools often provided an helpful guidance to narrow the compositional spectrum of ES ceramics in view to fabricate them [7] [18] [19] [20]. The successful fabrication of new multi-element ES materials (previously predicted) allows to measure key characteristics such as the structure and the composition. Paying greater attention to the topic of the present article, Y-P. Wang *et al*., combined special quasi-random structures model with the density-functional theory (DFT) within the generalized gradient approximation (GGA) and studied the mechanical and electronic properties of various ES borides [20]. The present work was able to

synthesize a single-phase ES diboride powder and the confirmation of the predicted structure enabled to exploit the DFT calculation and their published outputs to better study its structural stability.

Though the "ES-UHTC" topic is rousing a plenty of interest, densification but even earlier their synthesis remain an arena of technological challenges in progress. The prototype of the historic work [10] published the fabrication of a new class of ES diboride solid solutions having an unique layered hexagonal crystal structure with alternating rigid two-dimensional (2D) boron nets and 2D layers of different metal cations randomly distributed. The earliest fabrication of ES diborides, in brief, involved a high energy mechanical co-milling of individual pure MeB_2 powders in equimolar proportions followed by densification through spark plasma sintering (SPS) for 5 min dwell time at the peak temperature of 2273 K and 30 MPa of linear applied pressure. Such results lifted the curtain on a prospect to spread the range of unexplored ES ceramics, not exclusively limited to borides, and likely characterized by unparalleled chemical, mechanical, thermal and electrical properties.

The sluggish diffusion rate, one of the four historic "core effects" claimed to tag a "high-entropy" material [12], entails an intrinsic difficulty in the synthesis and densification of single phase and pore-free bulks, most notably when ES-UHTCs are involved. Residual porosity and secondary phases have been clarified being source of discrepancy between expected and measured properties. For this simple reason, Y. Zhang *et al*., managed to get fully dense high-entropy boride ceramics with ultra-high hardness adopting a boro-thermal approach of pure and highly energy ball milled oxide precursors followed by SPS for 10 min at 2273 K, 30 MPa of applied pressure: as reported in the text, in such conditions a final relative density of 99.2% was achieved [21]. L. Feng co-authored a very interesting work [8] where it was clearly shown that the fabrication of

single phase ES ceramic carbides obtained via carbo-thermal reduction implies lower-temperature processing conditions if compared to analogous diborides [21].

The palette of potential approaches to produce ES diboride SS bulks can actually be more colorful, ranging from processing mixtures of pure metals [22], or blending together pure Me-carrying compounds in the form of oxides [15] [23] [24] or even carbides [25]. An important turning point is the way to supply metalloids such as boron and carbon. Restricting the range of various options to the topic of the present contribution, some studies addressed ES diboride SS powders in the (Hf, Nb, Ta, Ti, Zr) system derived from a carbo-boro/thermal (CBT) reduction of transition metal (TM) oxides [15] [23][24]. Y. Zhang and co-workers started from TM oxides, boron carbide and graphite and managed to fabricate ES diboride SS ceramics by SPS at 2273 K [26]. J. Gu *et al*., prepared equimolar quinary (Hf,Nb,Ta,Ti,Zr)B_2 powders by CBT reduction at 2073 K in vacuum of TM oxides adding B_4C as source for B and C [23]. Phase-pure ES (Zr,Hf,Nb,Ta,Ti)B_2 powders were synthesized using a two-step process consisting of boro/carbo-thermal reduction followed by solid solution formation after heating to 2273 K, 0.3 wt% residual content of O and C [24]. In addition, to the best of the author's knowledge, the published literature presents two similar compositions (not the same) where amorphous boron was the main constituent of an oxide-based powder mixture [21], or of only a metallic-based one [22]. Tallarita *et al*., [22] in fact reported a two-step processing route, coupling self-propagating high-temperature synthesis (SHS) and SPS, to fabricate a single phase (Hf,Nb,Ta,Ti,Zr)B_2 SS bulk.

"One-step" experiments, i.e., those conducted to seamlessly process metal oxide precursors and get dense ES diborides, were till now not reported in the published literature. The critical point to allow for the volatile by-products developed during high temperature synthesis to escape rapidly the closed powder bed container (typical of SPS and hot-pressing) remained unsolved. The feasibility of a "one-step" vs a "two-step" synthesis to fully consolidate a dense bulk was in fact

object of the authors recent research, but not the matter of this contribution. Indeed, the present work, on one end, primarily addressed phase evolution and final synthesis of a AlB_2-type single phase ES diboride SS in the (Hf,Nb,Ta,Ti,Zr) system. On second end, the micro-strain intended as the compositional disorder of the ES multi-component material was analyzed by x-ray diffraction and discussed.

2. Experimental processes and characterizations

The present work was to develop a synthesis route for single phase $(Hf,Nb,Ta,Ti,Zr)B_2$ SS powders with a specific surface area (s.s.a) of about 1.5 m^2/g, or higher: such range corresponds to a spherical particle size of 0.5 μm (or lower) for a theoretical density of 8.34 g/cm^3 [10]. Diboride SS powders in the (Hf,Nb,Ta,Ti,Zr) system were produced through a route that consisted of a solid-state carbo-boro/thermal (CBT) reduction of TM oxides and further solid solution (SS) formation. The overall CBT reduction is summarized by the ideal reaction (1)

$$0.2\ TiO_{2(s)} + 0.2\ ZrO_{2(s)} + 0.1\ Nb_2O_{5(s)} + 0.2\ HfO_{2(s)} + 0.1Ta_2O_{5(s)} + 2\ B_{(s)} + 2.2\ C_{(s)} =$$
$$0.2TiB_{2(s)} + 0.2\ ZrB_{2(s)} + 0.2NbB_{2(s)} + 0.2\ HfB_{2(s)} + 0.2TaB_{2(s)} + 2.2\ CO_{(g)} \qquad (1)$$

while reaction (2)

$$0.2TiB_{2(s)} + 0.2\ ZrB_{2(s)} + 0.2NbB_{2(s)} + 0.2HfB_{2(s)} + 0.2TaB_{2(s)} = (Ti_{0.2}Zr_{0.2}Nb_{0.2}\ Hf_{0.2}Ta_{0.2})B_{2(s)} \quad (2)$$

ideally describes the formation of the targeted solid solution. Hafnium oxide (HfO_2, 99%, -325 mesh; Alfa Aesar), zirconium oxide (ZrO_2, 99%, grade SC101, mean size 0.8 μm, MEL Chemicals), titanium oxide (TiO_2, 99.9%, grade P25, mean size 20 nm, Degussa), tantalum oxide (Ta_2O_5, 99.85%, -325 mesh, Alfa Aesar), niobium oxide (Nb_2O_5, 99.9%, -325 mesh, Sigma-Aldrich), carbon black (C, grade BP 120, 30 m^2/g, Cabot) and amorphous boron (B, 95-97%,

Tradium GmbH, Germany) were used as starting materials: purity and typical sizes are declared according to the producers datasheets.

According to reaction (1), stoichiometric molar amounts of TM oxides and C were used. However, the molar amount of B was increased from the stoichiometric value of 2 up to 3.2 to compensate for any B lost during processing. Powder batches were comminuted and intimately homogenized using a high-energy planetary ball milling (HEPM, Fritzsch Pulverisette 6 - Germany) for 90 min under wet conditions of anhydrous ethyl alcohol, with spherical balls (2 mm diameter) and jar both made of Y-stabilized zirconia. HEPM was completed in 6 cycles consisting of 15 min comminution (400 rpm) interrupted by 10 min resting pauses to limit overheating. Preparatory HEPM tests allowed to estimate the expected contamination of zirconia by measuring the total weight of jar + balls before and after increasing milling times: in this way, the weighted content of each TM oxide was adjusted to equi-molarity taking into account the excess in zirconia introduced during HEPM. After HEPM, powder mixtures were let dry overnight at 353 K in a ventilated kiln, passed through a 150 μm mesh metallic sieve and then stored in a evacuated desiccator prior to further handling. After sieving, to improve particle contact, promote reaction, and suppress loss of powder during processing, 2 g of powder mixture were pre-compacted into a disk (10 mm diameter) under a uniaxial pressure of 3 MPa, and then cold isostatic pressed up to 300 MPa. Various disks coming from the same batch were placed in a graphite crucible, which in turn was coaxially inserted into a larger graphite die (inner diameter 60 mm). The sample-crucible-die assembly was then heated under vacuum (10-100 Pa) using an inductively heating system: ramps of 70 K/min up to 2173 K and final isothermal dwells were mastered by measuring the temperature on the outer wall of the graphite die using a two-color pyrometer. The cited assembly was arranged to allow for an unimpeded removal of gaseous by-products released during the synthesis and taken away thanks to the vacuum pumping system of the furnace vessel.

To optimize the B:C molar ratio (BCMR) and the temperature range at which reaction 1 (i.e., CBT reduction) and reaction 2 (solid solution formation) reach the best yield, various thermal treatments under vacuum were done at 1923, 2023, 2073, 2123 and 2173 K for 60 min, dwelling for 30 min at 1723 K. The mass change of various powder mixtures was measured before and after their respective heat treatment. The composition of a certain powder batch and its processing temperature (see Table 1) were labeled as HEPM-xx-yyyy where xx and yyyy indicate, respectively, BCMR and max. processing temperature. Synthesis and SS formation were further studied at lower temperature from room temperature to 1823 K using a cold compacted 10 mm disk made from HEPM-1.3 batch and an analytical thermo-balance (STA 449C/4/G Jupiter, NETZSCH Geratebau– Germany) in flowing Ar, 5 K/min heating rate.

Table 1. Classification of various powder batches produced, B:C molar ratio (BCMR), max. processing temperature (T_S), final isothermal dwell (t_S), and relative mass loss (Δ)

Batch	BCMR	T_S, K	t_S, min	Δ, %	Remarks
HEPM-0.9-1923	0.91	1923	60	30.2	VC
HEPM-0.9-2023	0.91	2023	60	30.4	VC
HEPM-0.9-2073	0.91	2073	60	30.7	VC
HEPM-0.9-2123	0.91	2123	60	31.5	VC
HEPM-0.9-2173	0.91	2173	60	31.0	VC
HEPM-1-1923	1.05	1923	60	31.8	VC
HEPM-1-2023	1.05	2023	60	32.3	VC
HEPM-1-2073	1.05	2073	60	34.4	VC
HEPM-1-2123	1.05	2123	60	32.8	VC
HEPM-1-2173	1.05	2173	60	36.5	VC
HEPM-1.1-1923	1.1	1923	60	31.1	VC
HEPM-1.1-2023	1.1	2023	60	31.3	VC
HEPM-1.1-2073	1.1	2073	60	33.4	VC
HEPM-1.1-2123	1.1	2123	60	32.4	VC
HEPM-1.1-2173	1.1	2173	60	36	VC
HEPM-1.3-1823	1.27	1823	0	32	TG
HEPM-1.3-2123	1.27	2123	60	35.2	VC
HEPM-1.5-2123	1.45	2123	60	35.2	VC

VC: vacuum range 10-100 Pa; TG: flowing Argon at 0.1 MPa

Thermodynamic calculations were performed using HSC software [27] assuming: - the activities of the condensed phases are one for both standard and non-standard state calculations; - the sum of various partial pressures of volatile by-products like $CO_{(g)}$ and $B_XO_{Y(g)}$ is equalized to the pressure in the working chamber. Neither intermediate diboride SS (which formed during heat treatment) nor the final equi-atomic one (see reaction 2) were taken into account for the thermodynamic considerations due to the lack of their thermodynamic data in the available database.

The as-treated powder batches were crushed using pestle and mortar, both made of Y-stabilized zirconia, and stored in a dry desiccator prior to further microstructure analysis. The specific surface area (s.s.a) was determined by the nitrogen adsorption analyzer (Surfer, Thermo-Fischer Scientific): the equivalent particle size was calculated from the s.s.a by assuming a spherical shape. Morphologies, representative particle size ranges and Z-contrast imaging of the as-synthesized powders were analyzed using a field emission (FE) scanning electron microscopy (FE-SEM, ZEISS Σigma – Germany) with a combination of secondary (SE) and back-scattered electron (BSE) detectors. Atomic percentages of metals were measured using FE-SEM equipped with a EDS detector (INCA Energy 300, Oxford Instruments - UK) at an accelerating voltage of 20 kV.

Phase analyses were done by x-ray diffraction (XRD, D8 Advance, Bruker - Germany), 2-theta step-size of 0.04° and 5 s dwell counting time, using Cu Kα radiation. The lattice parameters of some indexed phases were determined by Rietveld refinement of XRD data using TOPAS software [28].

To extrapolate the XRD peak broadening $\beta_{S,hkl}$ due to the microstructure of the sample, a best fitting of the instrumental broadening $\beta_{I,\theta}$ vs theta angle θ was first determined using a NIST

660b LaB_6 standard under the same conditions used for the (powder) sample. Effective $\beta_{S,hkl}$ values were thus determined for various Bragg peaks in accordance with the relation (3)

$$\beta_{S,hkl} = \sqrt{\left(\beta^2_{M,hkl} - \beta^2_{I,\theta}\right)} \quad (3)$$

where $\beta_{M,hkl}$ is the measured XRD peak broadening. In the current analysis, the $\beta_{I,\theta}$ vs θ best fitting was computed with a supposed Gaussian-like shape of peaks generated by the standard LaB_6. Adopting the Williamson-Hall analysis model [29], it is possible to get information on defects present in the sample. It was assumed that peak broadening due to average domain size (D) and micro-strain (ε) is Lorentzian, so that the integral breath of both β components are additive and contribute to β_S

$$\beta_{S,hkl} = 4 \cdot \left(\sqrt{\langle \varepsilon^2 \rangle}\right) \cdot \tan\theta + \frac{K \cdot \lambda}{D \cdot \cos\theta} \quad (4)$$

where K is a constant (dependent on the grain shape and orientation), λ is the incident x-ray wavelength, and $\sqrt{<\varepsilon^2>}$ the root mean square. Rearranging Eq. 4 gives:

$$\beta_{S,hkl} \cdot \cos\theta = 4 \cdot \left(\sqrt{\langle \varepsilon^2 \rangle}\right) \cdot \sin\theta + K \cdot \frac{\lambda}{D} \quad (5)$$

The slope of a linear fit to the plot of $\beta_{S,hkl} \cdot \cos\theta$ against $\sin\theta$ depends proportionally to only ε whereas the y-intercept of a linear fit with zero estimates D. Since the samples analyzed were supposed strain-free, the slope of the linear fit obtained by equation 5 can be interpreted as the relative variation of the inter-planar distances d_{hkl} due to the chemical inhomogeneity for the long range coexistence of metallic species with differing chemistry and atomic radius. An anisotropic $\beta_{S,hkl}$ peak broadening of the principal plane families (h00) and (00l) was differentiated by best fitting its different dependence from the Bragg diffraction angle.

3. RESULTS and DISCUSSION

This work shed light upon the sequence of chemical reactions which led to the successful solid state synthesis of entropy stabilized (ES), sub-micron and single phase (Hf,Nb,Ta,Ti,Zr)B_2 SS powders. Depending on the processing temperatures and the adjusted B:C molar ratios (BCMR) per one molar mass of various TMs, two intermediate AlB_2-type diboride solid solutions (labeled SS-HZB and SS-TNTB) as well as a rock-salt type cubic metal carbide SS (labeled SS-MeC) were identified until the starting TM oxides were fully converted into the desired ES (Hf,Nb,Ta,Ti,Zr)B_2 SS, hereafter labeled ES-MeB. Figure 1 shows an example for the positions of various indexed products. The XRD analysis of the heat-treated powder batches listed in Table 1 allowed to sort a predominance of the phases formed based on the strongest peak intensity, and thus was visually mapped in Fig. 2 together with the remaining oxides.

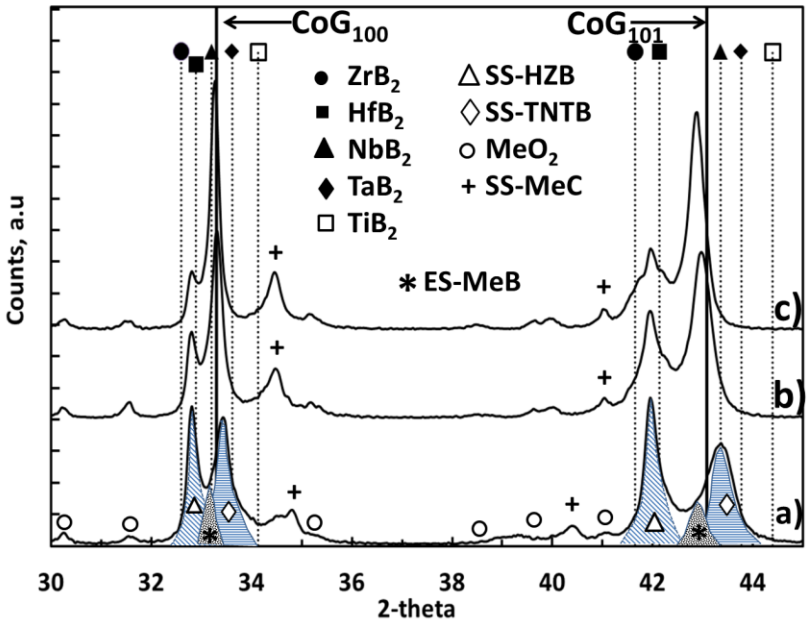

Figure 1. XRD patterns (background and $k_{\alpha 2}$ component stripped away) of HEPM-0.9-1923 (a), HEPM-0.9-2123 (b) and HEPM-0.9-2173 (c). In HEPM-0.9-1923, peaks [100] (≈32°-34° 2-theta) and [101] (≈41°-44° 2-theta) are visually sketched for SS-HZB, SS-TNTB and ES-MeB. The ideal positions for each individual MeB_2 and their center-of-gravity (CoG) are plotted.

In HEPM-1.3-2123 and HEPM-1.5-2123, the only indexed phase was ES-MeB. For the representative HEPM-1.3-2123 sample whose XRD pattern is plotted in Fig. 3, the full sequence of experimental XRD peaks was indexed and refined under the hypothesis of a single AlB_2-type crystalline phase: some outputs of the Rietveld refinement are reported in Table 2 and compared to literature data of the only (Hf,Nb,Ta,Ti,Zr)B_2 system. Some geometrical bond lengths were calculated according to the cell parameters reported in the relative cited reference: slight differences in the cell parameters may be ascribed to some departure from the ideal equimolar concentration of TMs present in the lattice.

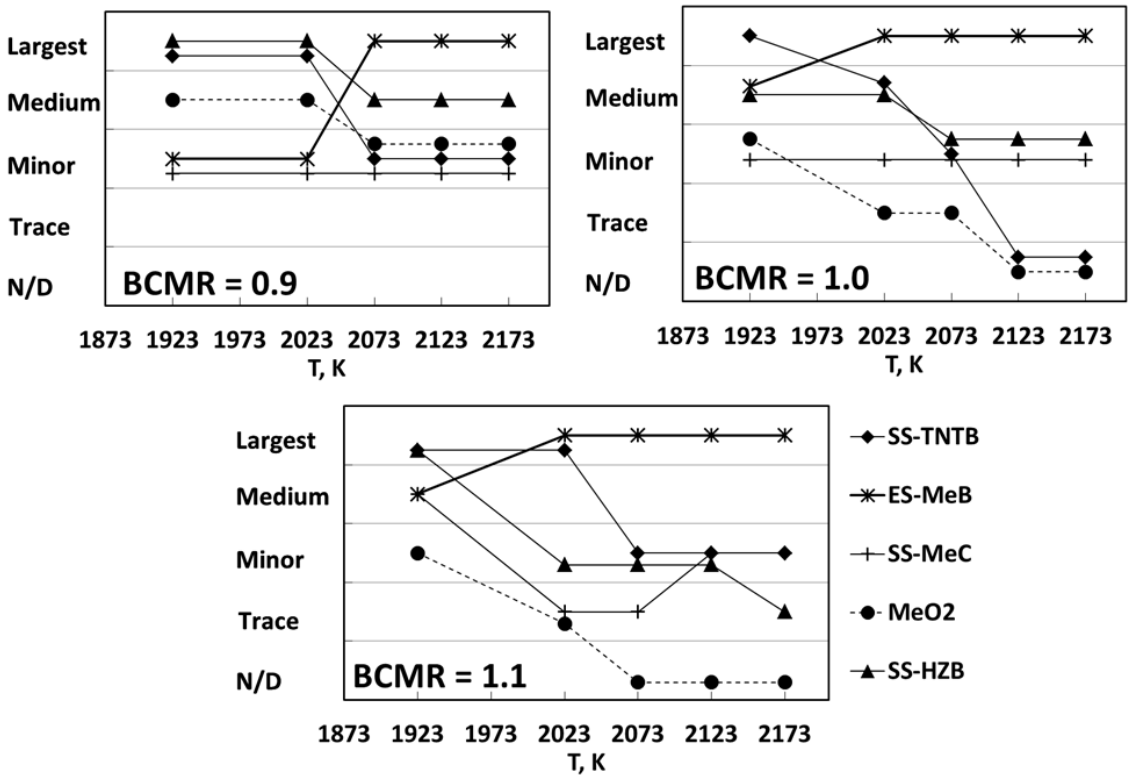

Figure 2. Various products were ranked over five bins (largest, medium, minor, trace, and not detectable N/D) comparing the intensity of their strongest peak: intermediate solid solutions SS-HZB and SS-TNTB, metal carbide SS-MeC and final targeted ES-MeB. Also residual oxides (MeO_2) were plotted.

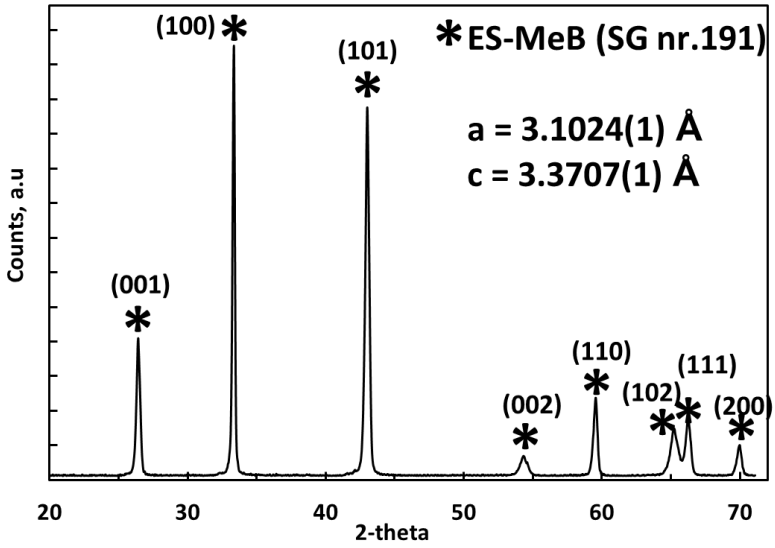

Figure 3. XRD pattern (background and $k_{\alpha 2}$ component stripped away) of HEPM-1.3-2123: a AlB_2-type phase, space group SG nr. 191, is the only indexed. The refined cell parameters are indicated.

Table 2. Comparison of main characteristics of HEPM-1.3-2123 (present study) and other published data: refined cell parameters a, c and lattice volume (V), geometrical bond length of Me-B and B-B, normalized atomic percentage of only metals (mean±1 st.dev. of 5 sampling rasters), density (ρ_{EQ}) calculated with an equimolar composition, or using experimental values (ρ_{EDS}), specific surface area (s.s.a.) and corresponding spherical particle size.

	Present Study	[23]	[24]	[15]	[10]	[26]	[20]	[30]
Sample status	Loose Powder	Loose powder	Loose powders	Porous Bulk	Sintered bulk	Sintered bulk	Calc.	Calc.
a, Å	3.1024(1)	3.1062(13)	3.105(8)	3.1036(1)	3.101	3.1033(3	3.116	3.104
c, Å	3.3707(1)	3.3755(21)	3.376(1)	3.3795(3)	3.361	3.3679(5)	3.391	3.364
c/a	1.087	1.087	1.087	1.089	1.083	1.089	1.088	1.084
V, $Å^3$	28.1	28.31	28.19	28.19	27.99	28.09	28.51	28.07
B-B , Å	1.7915	1.7937	1.793	1.7922	1.7907	1.7920	1.7994	1.7924
Me-B, Å	2.4595	2.4627	2.4624	2.4630	2.4556	2.4589	2.4722	2.4579
Ti, mol %	19.1±0.1	20	20	20	20	20	20	20
Zr, mol %	19.2±0.3	20	20	20	20	20	20	20
Nb, mol %	20.6±0.2	20	20	20	20	20	20	20
Hf, mol %	20.8±0.4	20	20	20	20	20	20	20
Ta, mol %	20.3±0.2	20	20	20	20	20	20	20
ρ_{EQ}, g/cm^3	8.27	8.24	8.24	8.24	8.32	8.27	8.15	8.28
ρ_{EDS}, g/cm^3	8.32	-	-	-	-	-	-	-
s.s.a., m^2/g	1.58	-	-	-	-	-	-	-
$d_{S,EQ}$ µm	0.46	0.4-0.6*	-	-	-	-	-	-
$d_{S,EDS}$ µm	0.45	-	-	-	-	-	-	-

*Estimated by SEM

Attention was also paid to the analysis of the anisotropic micro-strain. In our reasoning, such a feature is not related to one of the historic core effects known as lattice distortion [12], i.e., to the accommodation of lattice parameters due to the relaxation of the new formed AlB_2-type SS into its stable equilibrium configuration, rather to the extent of the compositional disorder caused by the occupancy of 2D-layered planes randomly filled of differing TM atoms. The section 3.4 was dedicated to this focus.

3.1 Thermodynamic considerations

The minimization of Gibbs' free energy of reaction (1) was calculated at non-standard conditions, and emphasized the beneficial effect of the vacuum in the working furnace vessel: besides reactants and products of reaction (1), also individual pure MeC, boron carbide (B_4C) and volatile boron oxides were considered in the product list. Thanks to the calculated equilibria vs temperature it makes sense that two sub-groups composed, respectively, of $\{TiB_2 + TaB_2\}$ and $\{ZrB_2 + HfB_2\}$ have different degree of conversion so that each sub-group started forming SS separately (Fig. 4). The role of Nb is more elusive compared to the remaining four TMs, and only a consistent B excess overcomes the competing reaction to form NbC in favor to NbB_2. Re-considering the results presented in Fig. 1, the two SS just mentioned were associated to SS-HZB and SS-TNTB. The temperatures at which the onset of each MeB_2 is predicted to become favorable decrease when the effect of the equilibrium total pressure is taken into account.

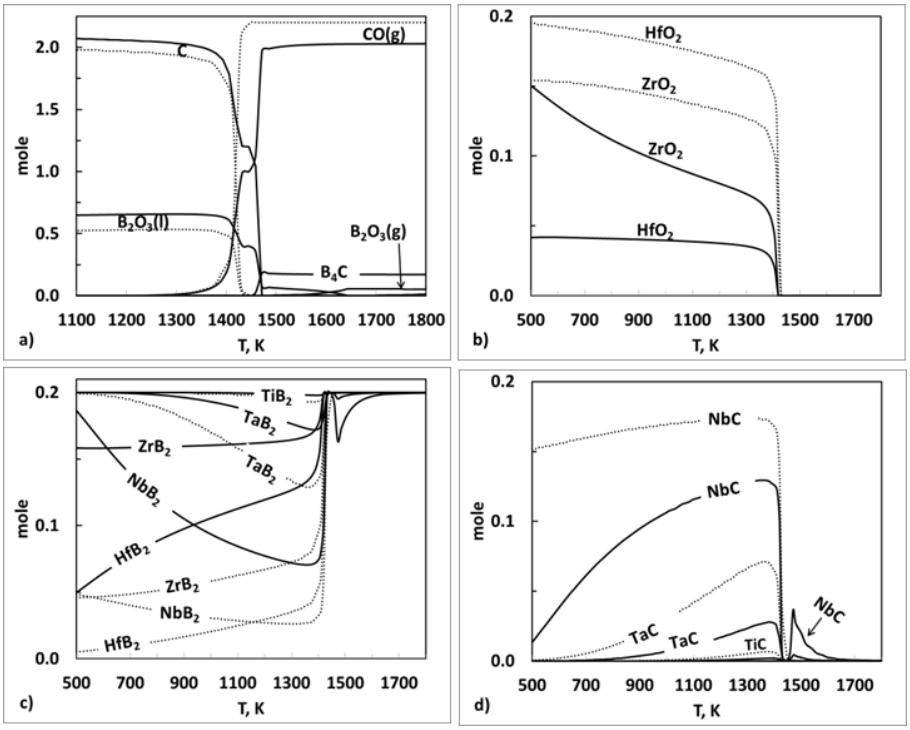

Figure 4. Equilibrium molar contents vs temperature (T) of relevant reactants and products of reaction (1) calculated via HSC software [27], 10 Pa of equilibrium pressure: dotted and full lines show trends, respectively, for BCMR=0.9 or 1.27.

The XRD analyses of various batches have never indexed individual MeB_2, rather in-situ synthesized MeB_2 already started reacting each other giving rise to new crystalline products which were indexed with a AlB_2-type structure, P_6/mmm (space group number 191). An example was proposed in Fig. 1. It is known that the individual MeB_2 and the related binary solid solutions share the same crystalline structure just mentioned. Therefore, in absence of complementary micro-analytical determinations, it is a plausible inference that the new intermediate crystalline phases SS-HZB and SS-TNTB are diboride SS of some TMs used in the starting composition, depending on their availability at different stage of reaction. In fact, although the actual composition of the metallic sub-lattice remains to be fully determined, it was deduced from a qualitative analysis of the XRD patterns that the inter-planar distances of principal Bragg planes (and thus the related chemical compositions) of SS-HZB, SS-TNTB, ES-MeB, and SS-MeC vary

vs. processing temperature (see Fig. 1). A practical rule of selection for the initial base composition of SS-HZB and SS-TNTB can be derived by minimizing the descriptor δ_X

$$\delta_x = \sqrt{\sum_{i=1}^{N} y_i \left(1 - \frac{x_i}{\bar{x}}\right)^2} \quad , \quad \bar{x} = \sum_{i=1}^{N} y_i x_i \qquad (6)$$

of some characteristics (x) like the atomic radius or the electronegativity, in general related to the coexistence of N different metallic atoms, y the molar concentration of each TM present. Based on the XRD analyses which excluded the presence of individual MeB_2, the probability for various MeB_2 to survive alone (i.e., not interacting with other metal diborides at temperature above 1823 K) was discharged. It means that separate MeB_2, once formed, start reacting each other selecting those binary (N=2) or ternary (N=3) compositions which minimize δ_X of key characteristics, some of them listed in Table 3. From the calculated values in Table 3 (obtained assuming a perfect solid solution model) it is intuitive that Nb, not being allowed to survive alone, prefers creating bonds with Ti and Ta (and not with Zr and/or Hf) whilst Hf and Zr together fulfill the minimization of various δ_x. In Table 3, other combinations for N=2, 3 and 4 were not reported because the corresponding δ_x values were all higher than those already listed for N=2 and N=3. However, data for N=5 and y=0.2 are reported for comparison purpose though well above the minima calculated for N=2 and N=3. In fact x-ray diffraction analyses showed that, increasing processing temperature above T= 2073 K, the ES-MeB phase with all the five transition metals is the only stable phase though its δ_x values are not minima. This is indeed the desired consequence of the entropy stabilization. The ideal Gibbs' free energy of mixing ΔG_{MIX}, $\Delta G_{MIX} = \Delta H_{MIX} - T \cdot \Delta S_{MIX}$, of the ES-MeB phase (space group P6/mmm with two sub-lattices termed "1a" and "2d" according to the Wickoff nomenclature) becomes fully dominated by the negative second term $T \cdot \Delta S_{MIX}$ which accounts for the augmented configurational entropy of mixing ΔS_{MIX}

$$\Delta S_{mix} = -R \frac{X}{X+Y} \sum_{i=1}^{N} x_i \ln(x_i) \qquad (7)$$

where R is the constant of gases, x_i the mole fraction of the i^{th} element in the "1a" sub-lattice which has X=1 as number of sites and N=5 is the element species. Y is equal to 2 because is the number of sites in the individual sub-lattice "2d" occupied only by B atoms: the "2d" sub-lattice does not contribute to increase the configuration entropy because x_1=1. Therefore ΔG_{MIX} expressed as

$$\Delta G_{MIX} = (2.72 - 4.456 \cdot 10^{-3} T) \qquad (8)$$

becomes negative above 600 K, where ΔH_{MIX} =2.72 kJ/mol is a calculated value [20]: it is assumed that the temperature dependence of ΔH_{MIX} of ideal/regular solid solutions remains very weak.

Compared to the as-prepared HEPM-0.9 powder batch, strictly speaking m-ZrO_2 and m-HfO_2 peaks in HEPM-0.9-1923 disappeared, and re-appeared reduced in intensity and merged together indicating a probable in-situ formation of a mixed (Zr,Hf)O_2. The CBT reaction (1) was also promoted by the $CO_{(g)}$ partial pressure in the working chamber kept low thanks to the pumping system.

Table 3. Descriptors (δx) of some characteristics calculated for ideal equi-molar solid solutions containing N metals, y=1/N: lattice parameters a and c, lattice volume (V) , atomic radius (r) and electro-negativity (e-neg)

Metal diboride SS	N	y	$\delta_{C/A}$, %	δ_V, %	δ_r, %	$\delta_{e\text{-}neg}$,%
Ti-Zr-Nb-Hf-Ta	5	0.2	2.0	6.5	4.7	8.1
Hf-Zr	**2**	**½**	**0.31**	**1.62**	**0.82**	**1.14**
Hf-Zr-Nb	3	1/3	1.9	4.5	4.05	9.6
Hf-Zr-Ti	3	1/3	1.82	7.45	4.62	7.68
Hf-Zr-Ta	3	1/3	1.97	5.65	4.6	6.4
Ti-Ta	2	½	0.17	2.05	0.03	1.32
Ti-Ta-Nb	**3**	**1/3**	**0.14**	**2.77**	**0.61**	**2.65**
Ti-Ta-Hf	3	1/3	1.76	6.1	4.3	7.3
Ti-Ta-Zr	3	1/3	2.06	7.65	5.1	6.3

As Fig. 4 has already clarified, another decisive compositional adjustment was the excess in B compared to the stoichiometric value predicted in accordance to reaction (1). The phase evolution for processing temperature raising from 1923 to 2173 K and other effects induced by the correction of BCMR are discussed in section 3.3.

3.2 Thermogravimetric analysis

A thermogravimetric test was performed using the HEPM-1.3 powder batch: this batch was judged the best candidate because its starting formulation combined to a processing temperature as low as 2123 K allowed to convert all the oxides and obtain the only pure ES-MeB phase (see Fig. 3). The relative mass loss (Δ) of HEPM-1.3-1823 was 32%: in Fig. 5, the relative mass change vs. temperature more clearly elucidates when the mass of the 10 mm disk begun changing noticeably.

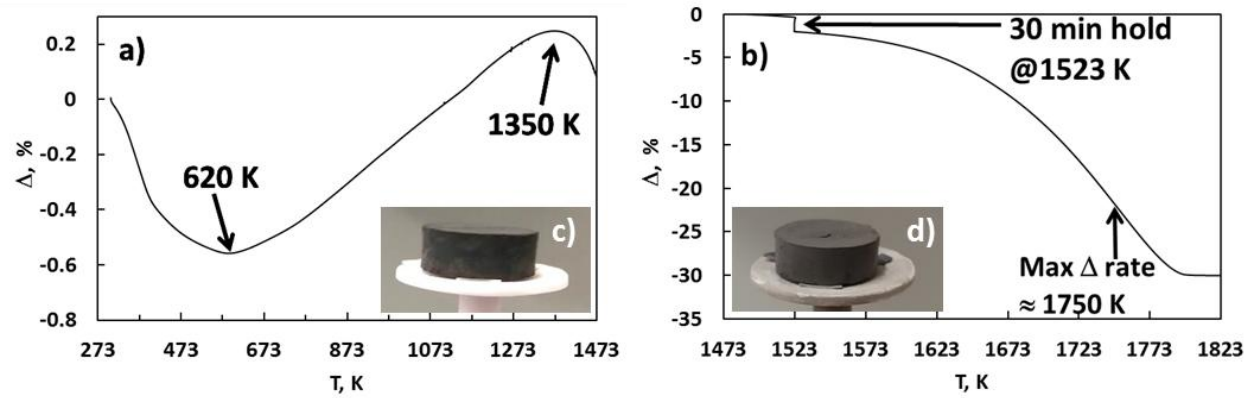

Figure 5. The HEPM-1.3 powder batch: the relative mass change (Δ) vs. temperature (T) is plotted up to 1473 K (a) and from 1473 K to 1823 K (b): around 1750 K the max. Δ rate was marked. The sample before (c) and after testing (d) is also shown.

If the mass loss up to about 620 K can be ascribed to residual solvent removal, the as gradual as modest mass gain up to about 1350 K was interpreted as oxidation of a minor quote of the added amorphous B. Actually, the most significant partt of the expected CBT reaction is marked above 1350 K when copious mass loss occurred (see Fig. 5b), reaching the max. Δ rate around 1750 K and fading away for temperature in excess of 1790 K. The onset temperature $T_{CO(g)}$ around 1320 K

marking the production of CO(g) nicely matches the local maximum in Fig. 5 where mass loss becomes the dominant mechanism to transport oxygen out of the system.

Phase analysis by XRD of HEPM-1.3-1823 (not reported in Fig. 2) indexed the formation of SS-HZB, SS-TNTB and ES-MeB but the conversion of the starting TM oxides remained not complete. The SS-MeC phase was not seen in HEPM-1.3-1823.

On one side, the overall mass loss of 32% apparently matches the theoretical value of 32.1% calculated from reaction (1). On the other side, phase identification by XRD has shown that reaction (1) did not proceed to full completion: it follows that, though the B:C molar ratio with excess B was adjusted, processing temperatures higher than 1823 K and reduced working pressure below 1 bar are necessary to bring precursors to the highest degree of conversion.

3.3 The carbo/boro-thermal reaction yield vs B:C starting molar ratio

It is readily understandable that the available overall contents of B and C influence the degree of conversion of the starting TM oxides into the targeted ES diboride SS (labeled ES-MeB). The possible use of B_4C powder alone as combined source for B and C does not allow to finely adjust the BCMR value as desired, unless you also add separately B and/or C. In the present work, starting powders of B and C were chosen amorphous and ultrafine in order to have strongly reactive precursors. In addition, B_4C is known to be very hard and then much more abrasive during HEPM than B and C alone: this may limit the uptake of material from the jar. The thermodynamic calculations foresee that, when B and C are added in stoichiometric molar amounts for reaction (1), the formation of TM diborides (pure or SS) competes versus the formation of some carbide counterparts. To confirm these predictions, the HEPM-0.9-yyyy series (see Table 1) was heat treated in vacuum (10-100 Pa) up to 2173 K, 60 min isothermal dwell. The

results showed that the overall CBT reaction was not complete and, besides the formation of the ES-MeB phase, other reaction products were clearly identified (see Fig. 2). The indications provided in Fig. 2 nicely match the former reasoning based on Table 3, that Zr and Hf readily react and give rise to the base composition of the AlB_2-type crystalline solid product labeled SS-HZB. In addition, those inter-planar d_{hkl} of the SS-HZB phase shown in Fig. 1 fall inside the sub-range delimited by the end-member ZrB_2 and HfB_2. In this regard, independently of the BCMR used, the seed of an "hosting structure" capable to accommodate all the five transition metals was at first identified to form at 1923 K, the lower limit of the synthesis temperature range throughout the present testing campaign. It was clear that three detectable AlB_2-type crystalline solid products of reaction (1) labeled SS-HZB, SS-TNTB and ES-MeB have formed, and were discriminated only for their common closed packed hexagonal symmetry (P_6/mmm) and related cell parameters. In this context, it is interesting to notice that no one of the crystalline structures of the initial TM oxides was kept as hosting structure for the ES-MeB product but a different one, i.e., hexagonal closed packed, was thermodynamically selected as most stable.

A decisive progress towards the products side of reaction (2), i.e., towards the formation of the targeted single phase ES diboride SS, took advantage by processing HEPM-1.1-yyyy, HEPM-1.3-yyyy and HEPM-1.5-yyyy at 2073 K and above. The HEPM-1.3-2123 sample was recognized as the best compromise of the current experimental campaign (see Fig. 3), because only one AlB_2-type phase (space group P_6/mmm) was indexed and thus identified as the targeted ES-MeB. In Fig. 6 a graphical representation is shown. The as-synthesized HEPM-1.3-2123 powder, gently crushed, had a s.s.a. of 1.58 m^2/g.

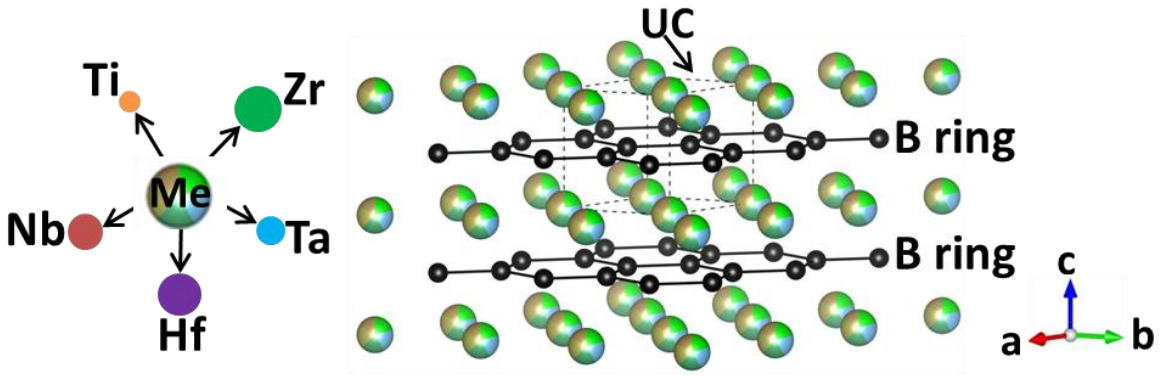

Figure 6. Graphical representation by VESTA [31] of the P_6/mmm hexagonal lattice (space group 191): Me positions are randomly occupied by Hf, Nb, Ta, Ti or Zr. B rings and an unit cell (UC) are also indicated.

SEM-EDS analyses were done to provide evidence that the as-synthesized HEPM-1.3-2123 powder is a multi-element diboride SS: in Table 2 relevant results of the coexistence of five metals in quasi-equimolar amounts are reported. Actually, a comparison with published data in Table 2 was not possible because only ideal (and not measured) equimolar contents of TM were reported. It should be noticed that, adjusting BCMR to 1.3 or higher, the threshold temperature at which the formation rate of the targeted ES-MeB SS powder greatly accelerated was 2073 K. It is expected that the resulting s.s.a. of the as-synthesized ES-MeB powders, together with an additional HEPM, would be beneficial to lower the densification temperature below 2373 K [10] [23] and likely get a fully dense single phase bulk.

To the best of the author's reasoning, the present work for the first time presents a CBT route as an approach to obtain single phase (Ta,Nb,Ta,Ti,Zr)B_2 SS powder using TM oxides, and elemental boron and carbon as initial reactants. In a recent work [26] Y. Zhang and co-authors reported the synthesis of ideal and equimolar single phase $(Ti_{0.2}Zr_{0.2}Nb_{0.2}Hf_{0.2}Ta_{0.2})B_2$ powders via carbo/boro-thermal reduction at 1873 K. Actually, by observing the published XRD patterns, the authors still detected and indexed residual oxides, meaning that the conversion of the initial TM oxides has not reached its full extent. However, J. Gu *et al*., showed that

$(Hf_{0.2}Nb_{0.2}Ta_{0.2}Ti_{0.2}Zr_{0.2})B_2$ powders were synthesized at 2073 K via CBT reduction of TM oxides and B_4C [23]: in this case the XRD pattern and the refined cell parameters match rather well those obtained in the current work.

By only increasing the absolute content of B over that of the stoichiometric C, the boro-thermal reaction of the TM oxides competes versus the CBT reduction. According to thermodynamic considerations, boron can be lost via release of volatile oxides so that some C, exempted from carrying oxygen out through CO(g), may remain unreacted and prone to form boron carbide. The low x-ray scattering factor of the atoms in the B_4C phase, compared to the heavier TM of the MeB_2, together with a possible poor crystallinity of the in-situ formed B_4C phase itself, might be at the origin of its failed detection via XRD analysis. Besides, a careful inspection via FESEM-EDS, in fact, revealed the presence of a lower Z phase (because of darker contrast in back-scattered electron mode). It is expected that boron carbide particles might remain trapped within the sintered microstructure of HEPM-1.3-2123 upon hot consolidation, eventually conferring an advantage of more hardness compared to a pure ES-MeB.

3.4 XRD analyses: structure determination, peak profile fitting and micro-strain

A special focus was dedicated to the HEPM-1.3-2123 powder batch and its XRD analysis. In particular, besides the Rietveld refinement to extract some key characteristics of the hexagonal closed packed (hcp) lattice (see Table 2), the peak profile analysis revealed a more pronounced sample peak broadening $\beta_{S,00l}$ compared to $\beta_{S,h00}$. For instance, at 2-theta = 54.34 and 69.95 deg., $\beta_{S,002}$ = 0.616 is much higher than $\beta_{S,200}$= 0.334 although the reflection 002 is positioned at lower 2-theta angle. Such result was associated to the compositional disorder caused by five differing transition metals which occupy randomly the metallic sub-lattice (1a Wickoff position) of the AlB_2-type structure (P_6/mmm, space group 191), see Fig. 7.

It was reported that Me-B bonds, whose crystallographic lengths were calculated (see Table 2), have mixed ionic/covalent characters [20] [18]. Within the "1a"sub-lattice of the 2D metal layers, Me-Me bonds undergo a distortion led by the more rigid second sub-lattice (2d Wickoff position) composed of six-membered graphitic like B rings: the periodicity of the 2D metal layers are therefore distorted towards a "strain free" value dictated by stronger σ-type B-B covalent bonds.

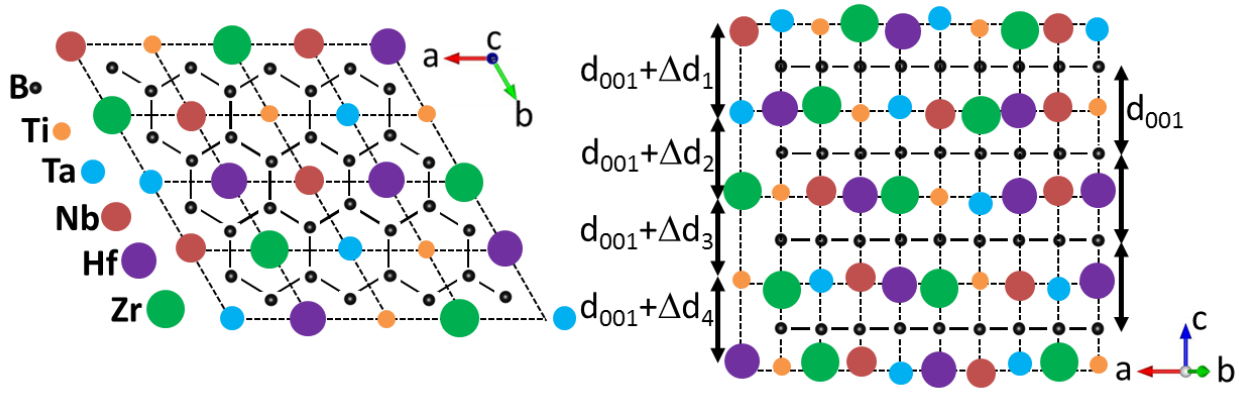

Figure 7. Visual representation of the disordered lattice due to metals with differing atomic size. The metallic sub-lattice, 1a Wickoff symbol, is occupied by the available five metals at random. Dashed segments connect the ideal 1a positions, Δd_n is the deviation from the d_{001} periodicity. B rings are plotted undistorted.

The electron density distribution was calculated via VESTA [31] and the colored maps in Figs. 8-9: clearly exhibit the predominance of the metallic, covalent or ionic-covalent bonds in certain zones of the crystalline arrangement.

SE-FESEM analysis of the as-synthesized ES-MeB powder pinpointed primary particles with obvious terraced nano-plates with a prevailing hexagonal shape (Fig. 10).

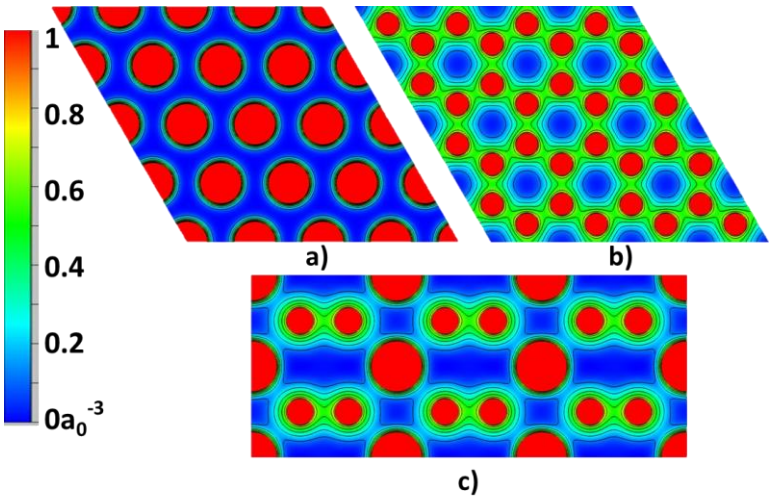

Figure 8. Three colored slices illustrating the 2D electron-density map of ES-MeB on plane parallel to (001) that are across Me (a) and B (b), and on plane (110) across both Me and B (c). Contours are plotted up to $1a_0^{-3}$, a_0 Bohr radius, with an interval of $0.1a_0^{-3}$.

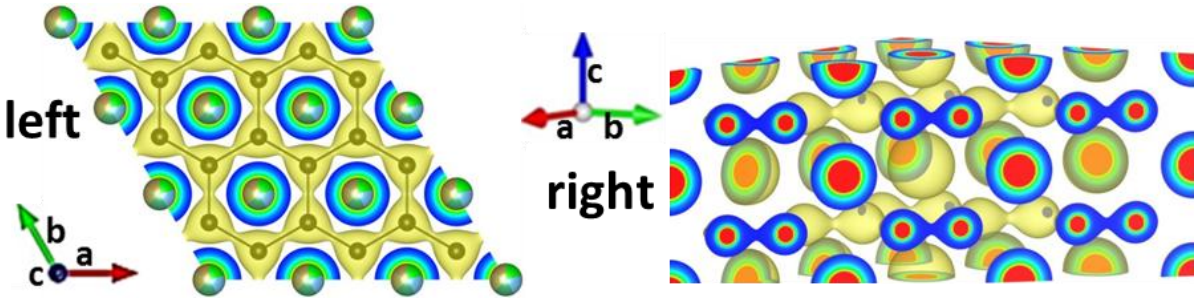

Figure 9. Electron-density distributions by VESTA [31] in ES-MeB and various hexagonal unit cells are shown with an iso-surface level of $0.6a_0^{-3}$, a_0 Bohr radius: left) 001 view with a "ball-and-stick" atomic structural model superimposed, right) general view with a cut-off plane (110). The strong covalent nature of the six-membered B rings and the ionic nature of Me-B bonds are visualized.

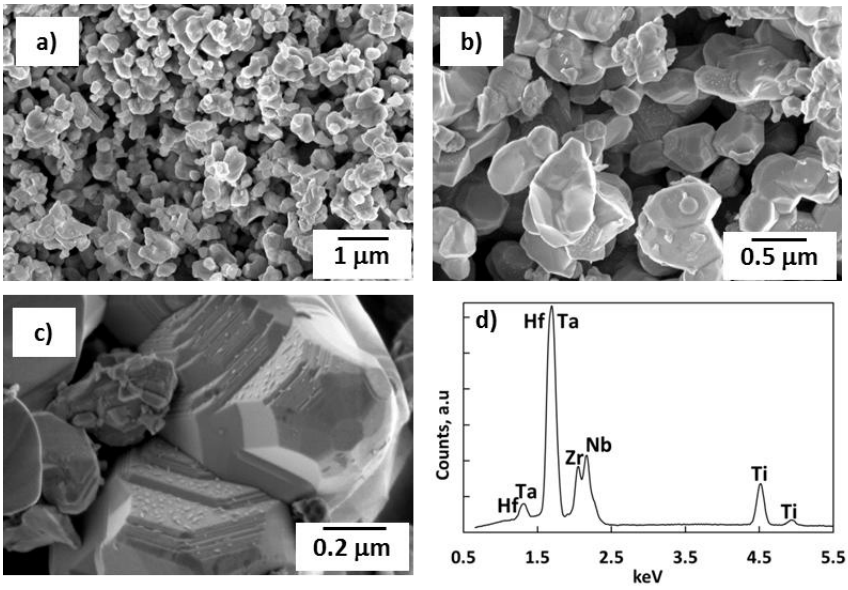

Figure 10. Morphology by SE-FESEM of the as-synthesized HEPM-1.3-2123 (a-c) and a FESEM-EDS spectrum acquired at 20 kV (d)

Coming back to the anisotropic sample peak broadening $\beta_{S,hkl}$, i.e., directly attributable to the microstructure of the sample, some arguments can be done. Dealing with a multi-element system, significant peak broadening was expected to occur eventually due to the micro-strain, in the present case ascribed to the variance in the inter-planar d_{hkl} throughout the sample. A commercial pure ZrB_2 powder (grade coarse, H.C. Starck – Germany) was used for comparative purposes. The extent of the micro-strain (ε) was evaluated by applying the analysis to the multi-element system (modeled like a single lattice structure) which was guessed strain-free by virtue of its actual status of powder slowly cooled down from the synthesis temperature. It follows that the best fitted value for ε (see equation 5) can be considered a measure of the deviation of d_{hkl} from the mean values (accommodated by the minimization of the internal energy) due to the compositional disorder (i.e., coexistence of five TM with differing atomic radii, bond strength and electronegativity). The scattered distribution of $\beta_{S,hkl} \cdot \cos\theta$ values in Fig.11a led to infer that a single ε does not fully implement the feature of the compositional disorder. The XRD pattern

covers a 2-theta range from 20° to 140° (a sector is shown in Fig. 11b) in order to get the greatest number of detectable Bragg reflections allowed by the Bragg-Brentano configuration used. A set of $\beta_{S,hkl}$ values were selectively taken and fitted for a linear regression model and ε values were obtained (see Fig. 11a): the corresponding goodness-of-fit R^2_{hkl} greatly improved (see Fig. 11a), when some families of reflections representing shared hkl directions in the crystal were grouped separately. These findings, in brief, signify that anisotropic $\beta_{S,hkl}$ values are compatible with the occurrence of a compositional disorder modeled in Fig. 7. To provide an order of magnitude for the inter-planar deviation δd along the equatorial or the axial direction, the calculated anisotropic micro-strain should be taken into account: the relative variation of the inter-planar distance $\delta d/d_{hk0}$ and $\delta d/d_{00l}$ have a value of about 1% and 2%, respectively. A compositional disorder, both structural and configurational, that may exist on the smallest crystalline length scale, i.e., B-B bond distortions and/or uneven Me distribution in the next nearest neighbor coordination spheres, unfortunately escapes the peak profile fitting described in Fig. 11 due to subtle variations that become averaged over longer sampling ranges.

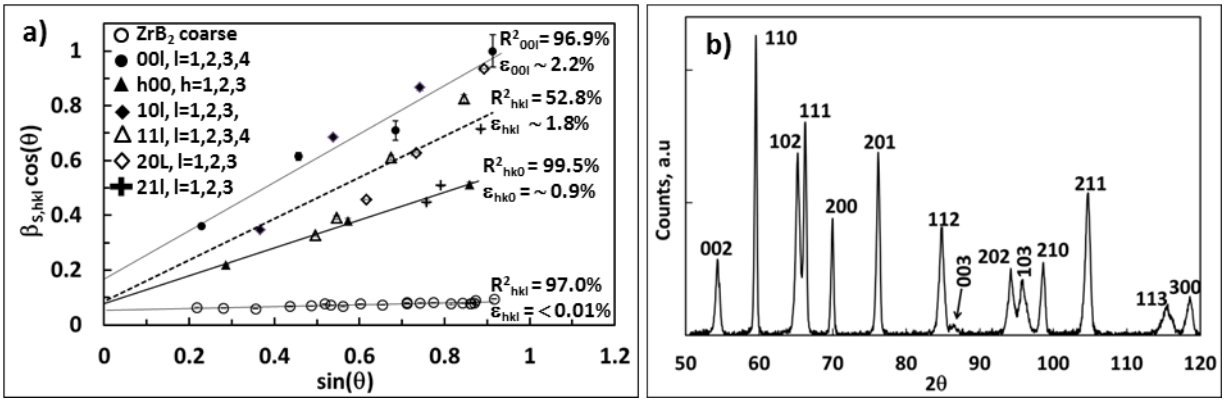

Figure 11. Williamson-Hall plot (a) showing goodness-of-fit (R^2) and estimated micro-strain ε for the principal family 00l and hk0; the overall R^2_{hkl} for all the indexed peaks belonging to ES-MeB and a commercial coarse ZrB_2 powder are indicated. In b) a relevant sector of the experimental XRD pattern of HEPM-1.3-2123 (background and $k_{\alpha 2}$ stripped away).

On the contrary, another measurable effect of lattice disorder, analogous to the thermal Debye-Waller effect but primarily due to chemical inhomogeneity, did not escape our XRD analysis, manifesting as a damping in the Bragg peaks intensities at increasing theta angles. In any case, quantitative analyses like extended x-ray absorption fine structure (EXAFS) [5] [16] or total scattering [32] are recommendable to in-depth study the local bond lengths of each cation-anion pairs and thus to better correlate the local disorder with properties.

Summary

A carbo/boro-thermal (CBT) reduction of transition metal (TM) oxides reacting with elemental B and C followed by solid solution formation was adopted to synthesize near equi-molar entropy stabilized (ES) AlB_2-type diboride SS powders in the Hf-Nb-Ta-Ti-Zr system. The starting B:C molar ratio per one molar mass of TM strongly influences the degree of conversion of TM oxides and further solid solution formation. Thermodynamic calculations and x-ray diffraction analyses agreed to indicate a grouping order of individual TM oxides and subsequent formation of two intermediate solid solutions in the $(Ti,Ta,Nb)B_2$ and $(Zr,Hf)B_2$ systems. High energy planetary ball milling (HEPM) helped a lot to homogenize the starting solid reactants and make them strongly reactive. Besides, only the addition of B in excess and processing temperatures ≥ 2123 K in vacuum allowed to complete the CBT process, and maximize the solid solution formation suppressing grain growth. The resulting $(Hf,Nb,Ta,Ti,Zr)B_2$ powders had a specific surface area of 1.58 m^2/g, and no detectable residual crystalline TM oxides.

XRD analyses assessed the ES diboride SS has a AlB_2-type lattice, space group number 191. The cell parameters were calculated via Rietveld refinement: a=3.1024(1) Å and c=3.3707(1) Å. SEM-EDS analyses on the as-synthesized SS powder verified the near equi-molarity of the five TMs present . A long-range periodicity model for the anisotropic micro-strain in the lattice was

proposed and confirmed by XRD analyses. The origin of such anisotropy was attributed to five differing TMs which randomly occupy strongly layered two-dimensional structures of the 00l planes.

Acknowledgements

The authors thank the colleagues D. Dalle Fabbriche and A. Sangiorgi for the high temperature testing campaign. The authors also acknowledge the generous support of Prof. William Fahrenholtz (Missouri Science & Technology University – Rolla, US) for helpful scientific discussion.

References

[1] E. Wuchina, E. Opila, M. Opeka, W. Fahrenholtz, I. Talmy, UHTCs: Ultra-High Temperature Ceramic materials for extreme environment applications, in: Electrochem. Soc. Interface, 2007.

[2] D. Sciti, L. Silvestroni, F. Monteverde, A. Vinci, L. Zoli, Introduction to H2020 project C3HARME–next generation ceramic composites for combustion harsh environment and space, Adv. Appl. Ceram. (2018). https://doi.org/10.1080/17436753.2018.1509822.

[3] F. Monteverde, J.M. Cordoba, R. Savino, A. Cecere, S. Genna, C. Leone, Thermal stability under laser heating of hot-pressed $(Hf_{1-X}\ Zr_X)B_2$/SiC powder mixtures obtained by mechano-synthesis, J. Eur. Ceram. Soc. 39 (2019) 4575–4587. https://doi.org/https://doi.org/10.1016/j.jeurceramsoc.2019.06.050.

[4] F. Monteverde, A. Cecere, R. Savino, Thermo-chemical surface instabilities of SiC-ZrB_2 ceramics in high enthalpy dissociated supersonic airflows, J. Eur. Ceram. Soc. 37 (2017). https://doi.org/10.1016/j.jeurceramsoc.2017.01.018.

[5] C.M. Rost, E. Sachet, T. Borman, A. Moballegh, E.C. Dickey, D. Hou, J.L. Jones, S. Curtarolo, J.P. Maria, Entropy-stabilized oxides, Nat. Commun. (2015). https://doi.org/10.1038/ncomms9485.

[6] R. Witte, A. Sarkar, R. Kruk, B. Eggert, R.A. Brand, H. Wende, H. Hahn, High-entropy oxides: An emerging prospect for magnetic rare-earth transition metal perovskites, Phys. Rev. Mater. (2019). https://doi.org/10.1103/PhysRevMaterials.3.034406.

[7] P. Sarker, T. Harrington, C. Toher, C. Oses, M. Samiee, J.P. Maria, D.W. Brenner, K.S. Vecchio, S. Curtarolo, High-entropy high-hardness metal carbides discovered by entropy descriptors, Nat. Commun. (2018). https://doi.org/10.1038/s41467-018-07160-7.

[8] L. Feng, W.G. Fahrenholtz, G.E. Hilmas, Low-temperature sintering of single-phase, high-entropy carbide ceramics, J. Am. Ceram. Soc. (2019). https://doi.org/10.1111/jace.16672.

[9] P.H. Mayrhofer, A. Kirnbauer, P. Ertelthaler, C.M. Koller, High-entropy ceramic thin films; A case study on transition metal diborides, Scr. Mater. (2018). https://doi.org/10.1016/j.scriptamat.2018.02.008.

[10] J. Gild, Y. Zhang, T. Harrington, S. Jiang, T. Hu, M.C. Quinn, W.M. Mellor, N. Zhou, K. Vecchio, J. Luo, High-Entropy Metal Diborides: A New Class of High-Entropy Materials and a New Type of Ultrahigh Temperature Ceramics, Sci. Rep. (2016). https://doi.org/10.1038/srep37946.

[11] J. Gild, J. Braun, K. Kaufmann, E. Marin, T. Harrington, P. Hopkins, K. Vecchio, J. Luo, A high-entropy silicide: $(Mo_{0.2}Nb_{0.2}Ta_{0.2}Ti_{0.2}W_{0.2})Si_2$, J. Mater. (2019). https://doi.org/10.1016/j.jmat.2019.03.002.

[12] D.B. Miracle, O.N. Senkov, A critical review of high entropy alloys and related concepts, Acta Mater. (2017). https://doi.org/10.1016/j.actamat.2016.08.081.

[13] R.Z. Zhang, M.J. Reece, Review of high entropy ceramics: design, synthesis, structure and

properties, J. Mater. Chem. A. (2019). https://doi.org/10.1039/c9ta05698j.

[14] S.R. Levine, E.J. Opila, M.C. Halbig, J.D. Kiser, M. Singh, J.A. Salem, Evaluation of ultra-high temperature ceramics for aeropropulsion use, J. Eur. Ceram. Soc. (2002). https://doi.org/10.1016/S0955-2219(02)00140-1.

[15] H. Chen, H. Xiang, F.Z. Dai, J. Liu, Y. Zhou, Porous high entropy $(Zr_{0.2}Hf_{0.2}Ti_{0.2}Nb_{0.2}Ta_{0.2})B_2$: A novel strategy towards making ultrahigh temperature ceramics thermal insulating, J. Mater. Sci. Technol. (2019). https://doi.org/10.1016/j.jmst.2019.05.059.

[16] B. Ye, T. Wen, Y. Chu, High-temperature oxidation behavior of $(Hf_{0.2}Zr_{0.2}Ta_{0.2}Nb_{0.2}Ti_{0.2})C$ high-entropy ceramics in air, J. Am. Ceram. Soc. (2020). https://doi.org/10.1111/jace.16725.

[17] L. Backman, E.J. Opila, Thermodynamic assessment of the group IV, V and VI oxides for the design of oxidation resistant multi-principal component materials, J. Eur. Ceram. Soc. (2019). https://doi.org/10.1016/j.jeurceramsoc.2018.11.004.

[18] T.J. Harrington, J. Gild, P. Sarker, C. Toher, C.M. Rost, O.F. Dippo, C. McElfresh, K. Kaufmann, E. Marin, L. Borowski, P.E. Hopkins, J. Luo, S. Curtarolo, D.W. Brenner, K.S. Vecchio, Phase stability and mechanical properties of novel high entropy transition metal carbides, Acta Mater. (2019). https://doi.org/10.1016/j.actamat.2018.12.054.

[19] B. Ye, T. Wen, K. Huang, C.Z. Wang, Y. Chu, First-principles study, fabrication, and characterization of $(Hf_{0.2}Zr_{0.2}Ta_{0.2}Nb_{0.2}Ti_{0.2})C$ high-entropy ceramic, J. Am. Ceram. Soc. (2019). https://doi.org/10.1111/jace.16295.

[20] Y.P. Wang, G.Y. Gan, W. Wang, Y. Yang, B.Y. Tang, Ab Initio Prediction of Mechanical and Electronic Properties of Ultrahigh Temperature High-Entropy Ceramics $(Hf_{0.2}Zr_{0.2}Ta_{0.2}M_{0.2}Ti0.2)B_2$ (M = Nb, Mo, Cr), Phys. Status Solidi Basic Res. (2018). https://doi.org/10.1002/pssb.201800011.

[21] Y. Zhang, W.M. Guo, Z. Bin Jiang, Q.Q. Zhu, S.K. Sun, Y. You, K. Plucknett, H.T. Lin, Dense high-entropy boride ceramics with ultra-high hardness, Scr. Mater. (2019). https://doi.org/10.1016/j.scriptamat.2019.01.021.

[22] G. Tallarita, R. Licheri, S. Garroni, R. Orrù, G. Cao, Novel processing route for the fabrication of bulk high-entropy metal diborides, Scr. Mater. (2019). https://doi.org/10.1016/j.scriptamat.2018.08.039.

[23] J. Gu, J. Zou, S.K. Sun, H. Wang, S.Y. Yu, J. Zhang, W. Wang, Z. Fu, Dense and pure high-entropy metal diboride ceramics sintered from self-synthesized powders via boro/carbothermal reduction approach, Sci. China Mater. (2019). https://doi.org/10.1007/s40843-019-9469-4.

[24] L. Feng, W.G. Fahrenholtz, G.E. Hilmas, Two-step synthesis process for high-entropy diboride powders, J. Am. Ceram. Soc. (2019). https://doi.org/10.1111/jace.16801.

[25] H. Zhang, D. Hedman, P. Feng, G. Han, F. Akhtar, Correction: A high-entropy $B_4(HfMo_2TaTi)C$ and SiC ceramic composite (Dalton Transactions (2019) DOI: 10.1039/c8dt04555k), Dalt. Trans. (2019). https://doi.org/10.1039/c9dt90099c.

[26] Y. Zhang, Z. Bin Jiang, S.K. Sun, W.M. Guo, Q.S. Chen, J.X. Qiu, K. Plucknett, H.T. Lin, Microstructure and mechanical properties of high-entropy borides derived from boro/carbothermal reduction, J. Eur. Ceram. Soc. (2019). https://doi.org/10.1016/j.jeurceramsoc.2019.05.017.

[27] A. Roine, HSC, (2017).

[28] TOPAS - Academic V6.

[29] G.K. Williamson, W.H. Hall, X-ray line broadening from filed aluminium and wolfram, Acta Metall. (1953). https://doi.org/10.1016/0001-6160(53)90006-6.

[30] S.M. Zheng, S.Q. Wang, Elastic properties of face-centered cubic, body-centered cubic and

hexagonal high entropy alloys by MaxEnt approach, Mater. Res. Express. (2018). https://doi.org/10.1088/2053-1591/aac67c.

[31] F. Izumi, K. Momma, Three-Dimensional Visualization in Powder Diffraction, in: 2007. https://doi.org/10.4028/3-908451-40-x.15.

[32] L.R. Owen, H.J. Stone, H.Y. Playford, The assessment of local lattice strains in alloys using total scattering, Acta Mater. (2019). https://doi.org/10.1016/j.actamat.2019.02.038.